Device

Article

Floating electricity generator for omnidirectional droplet vibration harvesting

Graphical abstract

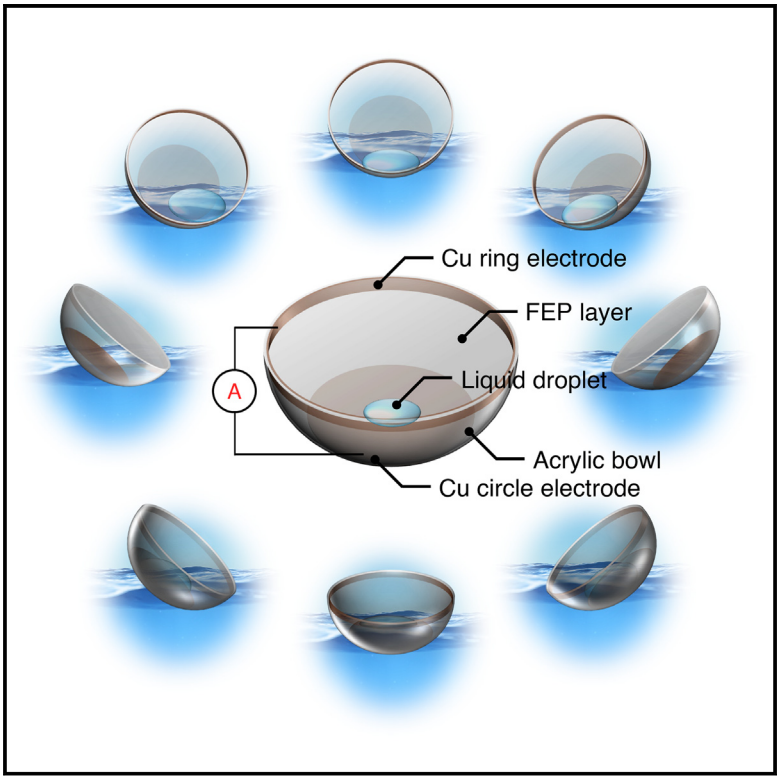

Highlights

- Floating electricity generator for omnidirectional mechanical energy harvesting
- The difference in capacitance formed on electrodes improves the electrical outputs
- The ion injection into the droplet enhances the amount of charge generated
- Omnidirectionality, stability, and scalability of the device were demonstrated

Authors

Jiaming Zhou (周家明), Xiaoting Ma (麻小挺), Zihao Deng (邓子豪), Jingyi Gao (高婧宜), Eunjong Kim (김은종), Hongjian Zhou (周宏建), Dong-Myeong Shin (신동명)

Correspondence

dmshin@hku.hk

In brief

Zhou et al. report a floating electricity generator featuring asymmetric capacitance on the electrodes. Instantaneous switching of a closed-loop circuit, together with asymmetric capacitance, increased the output voltage and current, while the amount of charge generated remains similar. The device can harvest low-frequency mechanical stimuli from all planar directions, with demonstrated stability and scalability.

3 Develop
Prototype with demonstrated applications in relevant environment

Zhou et al., 2025, Device *3*, 100653
April 18, 2025
https://doi.org/10.1016/j.device.2024.100653

CellPress

Device

CellPress
OPEN ACCESS

Article

Floating electricity generator for omnidirectional droplet vibration harvesting

Jiaming Zhou (周家明),[1] Xiaoting Ma (麻小挺),[1] Zihao Deng (邓子豪),[2] Jingyi Gao (高婧宜),[1] Eunjong Kim (김은종),[1] Hongjian Zhou (周宏建),[3] and Dong-Myeong Shin (신동명)[1,4,*]

[1]Department of Mechanical Engineering, The University of Hong Kong, Pokfulam Road, Hong Kong, China
[2]Department of Chemistry, The Hong Kong University of Science and Technology, Kowloon, Hong Kong, China
[3]Key Laboratory of Materials Physics & Anhui Key Laboratory of Nanomaterials and Nanotechnology, Institute of Solid State Physics, Hefei Institutes of Physical Science, Chinese Academy of Sciences, Hefei 230031, China
[4]Lead contact
*Correspondence: dmshin@hku.hk
https://doi.org/10.1016/j.device.2024.100653

THE BIGGER PICTURE Harvesting open ocean energy can be used to power devices that need to be deployed in the ocean without access to the power grid, such as Internet of Things (IoT) devices for environmental monitoring. Triboelectric nanogenerators (TENGs) have been explored for energy harvesting in open ocean environments, but most TENGs suffer from wear and tear issues due to specific working mechanisms. Droplet-based TENGs have received attention due to their advantage of having a low friction nature, enabling durable and sustainable energy harvesting from slow mechanical energy resources. However, most droplet-based devices can only harvest mechanical energy along a single direction, which is not favorable for unpredictable open ocean environments. Here, we report a floatable-droplet-based TENG harvesting natural wave energy from all directions. Our TENG outperforms conventional floatable TENGs in power and charge densities, opening up an avenue for ocean energy harvesting.

SUMMARY

There has been a surge of interest in droplet-based triboelectric nanogenerators, facilitating the durable and sustainable harnessing of slow and periodic mechanical energy resources. A major challenge faced by most of these devices is the concurrent achievement of high electrical outputs and omnidirectionality, which hampers their immediate implementation in real-world slow and periodic energy harvesting scenarios. We present a floating-droplet-activated electricity generator featuring asymmetric electrodes together with the switching of an internal circuit, with a current output of ~107.6 μA, a power density of 1.2 kW/m^3, and a charge density of 31.2 mC/m^3. When multiple devices were parallelly integrated, the current output reached 1.2 mA at a waving frequency of 0.28 Hz. Furthermore, the omnidirectionality and stability of the device have been examined, demonstrating that our device is applicable in any marine conditions and can harvest sustainable and extensive energy from natural vibrations.

INTRODUCTION

Triboelectric nanogenerators (TENGs) exploit low-frequency mechanical stimuli with an energy conversion efficiency as high as 70.6%[1–3] and can convert ambient mechanical energy into electricity. Numerous architectures, such as ball-embedded,[4–12] liquid-activated,[13–16] pendulum-employed,[17–20] and spring-assisted[21–24] types, have succeeded in harvesting mechanical energy with low frequencies to date. Droplet-based TENGs have the advantage of a nearly frictionless triboelectric interface,[25] enabling durable and sustainable energy harvesting from slow and periodic mechanical energy resources. However, most devices have struggled to simultaneously achieve a high output voltage of >300 V and an output current of >100 μA. Much effort has been devoted to boosting the output using different strategies: by optimizing the droplet position,[26] dielectric materials,[27,28] droplet injection speed,[29] droplet contact area,[30] and electrode design[31–33] and precharging the droplets.[34,35] State-of-the-art droplet-based electricity generators have achieved instantaneous output voltages and currents up to approximately 2,000 V and 4,000 μA,[35] with the help of liquid droplets in direct contact with an electrode. Although TENGs with solid-solid interfaces have strived to achieve

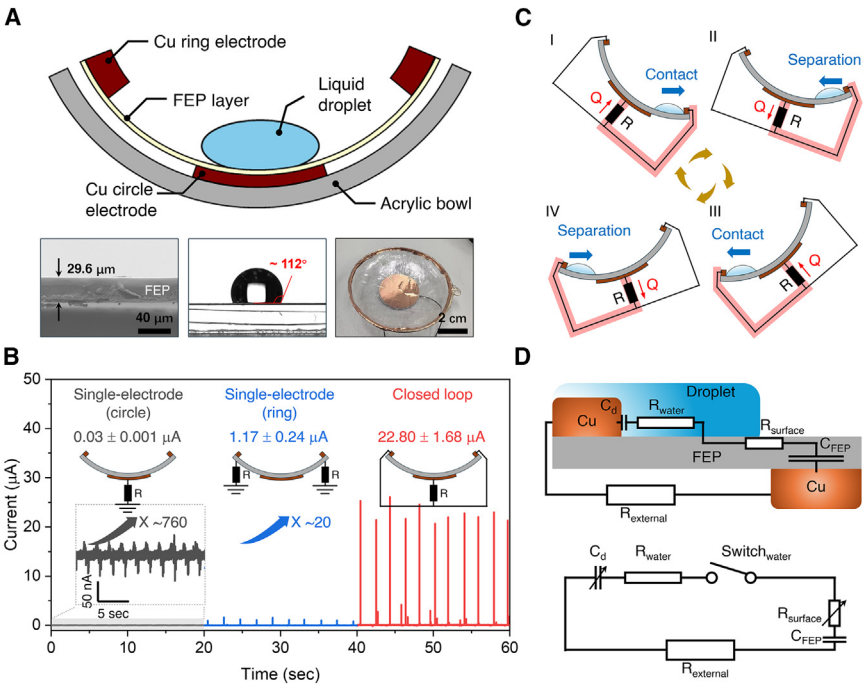

Figure 1. Overview of the FDEG

(A) Schematic of the floating-droplet-activated electricity generator (FDEG). The insets show the thickness (bottom left) and hydrophobicity (bottom middle) of the contact-electrification layer (FEP) and an optical image of the device (bottom right).

(B) The output currents measured from the FDEG with three different configurations for electrical connections (in dark gray: single-electrode configuration to the circular electrode, in blue: single-electrode configuration to the ring electrode, and in red: closed-loop configuration) under the same waving frequency of 0.28 Hz and DI water droplet volume of 2.4 mL.

(C) Schematic diagram of the working principle of the FDEG.

(D) Equivalent circuit model of the FDEG.

omnidirectional energy harvesting in light of the unpredictable nature of low-frequency mechanical stimuli,[4,5,10,13,26] most droplet-based devices can only harvest mechanical energy along a single direction, limiting their direct application in practical slow and periodic energy harvesting.

We present a floating droplet vibration-activated electricity generator characterized by the disparity in capacitance on the electrodes. The switching of the internal circuit, in conjunction with the difference in capacitance, facilitates the dramatical increase in the output voltage and current magnitude while maintaining consistent charge generation. This simple design exhibits practical advantages for wave energy harvesting from the perspective of omnidirectionality, cost, performance, and scalability, which could potentially serve as an individual unit of TENG toward large-scale open ocean energy harvesting.

RESULTS AND DISCUSSION

Design and fabrication of the FDEG

The floating-droplet-activated electricity generator (FDEG) is composed of two layers (Figure 1A, middle). The inside layer is a thin electricity generator comprising a circular fluorinated ethylene propylene (FEP; Figure 1A, bottom left) film along with ring and circular Cu electrodes at the circumference and center, respectively. The outside layer is a supporting acrylic hemispheric bowl, keeping the electricity generator afloat and being rocked by the water waves (Figure 1A, middle). A deionized (DI) water droplet, which serves as a counter-contact electrification material, is embedded on the top of the FEP layer, in which the hydrophobicity of the FEP layer facilitates the rolling of the droplet during movement (Figure 1A, bottom middle). The ring electrode positioned on the top of the FEP layer allows direct contact with a droplet, while the circle electrode located underneath the FEP layer is secured to avoid direct contact with the droplet. The thin electricity generator is bonded to the acrylic bowl surface to seal the surface, protecting the circular electrode from getting wet (Figure 1A, bottom right).

The asymmetric exposure of electrodes to water is a critical factor in providing sharp voltage and current outputs. Figure 1B shows the current output of the FDEG with a closed-loop configuration, in which the droplet bridges the ring and circle electrodes, allowing charge flow throughout the FDEG internal circuit system. A DI water droplet of 2.4 mL was oscillated over the FEP surface, driven by a swing motor with a frequency of 0.28 Hz (Figure S1). The FDEG yields an instantaneous current output of 22.80 ± 1.68 μA, which is approximately 760 and 20 times greater than the values obtained from single-electrode configurations with either circular or ring electrodes only, respectively. The FDEG has shown no noticeable current output when the droplet rolls over the FEP surface. Upon touching the ring electrode with the droplet, the current rises to 25.3 μA (Figure S2A), as the droplet turns on the switch of the internal closed-loop circuit in the FDEG. Then, there is a drop in the current with a full width at half maximum (FWHM) of 0.16 ms, indicating rapid charge redistribution throughout the closed loop. Note that an instantaneous increase in the current has also been achieved in the single-electrode configuration with the ring electrode (FWHM = 0.193 ± 0.003 ms), whereas the single-electrode configuration with the circle electrode shows a slow charge redistribution (FWHM = 220 ± 24 ms), implying that direct contact between the ring electrode and the droplet plays an essential role in instantaneous output. For the separation current peak, a gradual increase up to 0.102 μA, followed by a steady decrease, was found when the contact area with the ring electrode started to decrease (Figure S2B). As seen in Figure S3, the transferred charges increase to 16.56 ± 0.39 nC at the moment of contact and then drop to zero after separation, suggesting that the amount of total transferred charge after saturation remains the same over the course of cycling.

The working mechanism of FDEG

When a water droplet touches either the FEP layer or ring electrode, the surface of the FEP layer or ring electrode accepts the negative charge from the droplet according to the triboelectric series.[36] The power generation process of the FDEG can be divided into four stages, as shown in Figure 1C. During the first stage (stage I), the droplet bridges the ring electrode and FEP layer on top of the circular electrode, switching on a closed-loop circuit and then switching off the circuit at the moment of separation from the circular electrode. During the second stage (stage II), the droplet slides toward the center of the FEP layer and reduces the contact area with the ring electrode while initiating an overlap with the circle electrode, gradually switching on the circuit. The circuit is switched off again when the droplet is separated from the ring electrode. At the third (stage III)and fourth (stage IV) stages, the process of switching on and off repeatedly occurs. In the on state, the charges (Q) are transferred through the external load (R) between two electrodes to balance their established potential. From the circuit perspective (see Figure 1D), the FEP layer on top of the circular electrode acts as a capacitor, C_{FEP}, where the surface charge develops after contact electrification, with the droplet acting as the top plate and the circular electrode acting as the bottom plate. The electrical double layer that forms at the interface between the droplet and the ring electrode can be considered a variable capacitor, C_d, whose value differs according to the contact area, while the droplet acts as the resistor and switch.

The circuit can be written as a capacitor discharging model with two capacitors and resistors (see Note S1). The time-dependent discharging current curve can be expressed as

$$(t) = \frac{Q_d C_{FEP} + Q_{FEP} C_d}{C_d C_{FEP} (R_{water} + R_{surface} + R_{external})} e^{\frac{-(C_d + C_{FEP})}{C_d C_{FEP} (R_{water} + R_{surface} + R_{external})} t},$$

(Equation 1)

where R_{water}, $R_{surface}$, and $R_{external}$ indicate the resistances of the water droplet, FEP surface, and external load, respectively. Given that the droplet makes a point contact with the electrode at the moment of switching on (stages 1 and 3), the capacitance of C_d is several orders of magnitude less than that of C_{FEP} so that the magnitude of the current and the discharging time can be simplified as $Q_d/(C_d(R_{water} + R_{surface} + R_{external}))$ and $C_d(R_{water} + R_{surface} + R_{external})$, respectively. Considering the high surface charge, Q_d, on the ring electrode together with the small C_d, a current peak and discharge occur when the droplet is in contact with the ring electrode. The equation fits the peak data very well, as shown in Figure S4. The fitted value of C_d was determined to be 1.79 ± 0.5 pF, which is two orders of magnitude lower than that of C_{FEP} and is consistent with the predictions of the circuit model. After the droplet makes complete contact with the ring electrode (stages 2 and 4), the capacitance of C_{FEP} becomes negligible compared with that of C_d while maintaining contact with the ring electrode, as the electrical double layer is much thinner than the FEP layer; therefore, the magnitudes of the current discharge time can be approximated as $Q_{FEP}/(C_{FEP}(R_{water} + R_{surface} + R_{external}))$ and $C_{FEP}(R_{water} + R_{surface} + R_{external})$, respectively. The C_{FEP} was found to be two orders of magnitude greater than that of C_d when the droplet makes contact, yielding a low current output and slow discharge compared to the outputs during stages 1 and 3. The gradual decrease in the contact area with respect to the ring electrode leads to a slow increase in the current peak while separating. We estimated the amount of charge transfer based on the proposed equivalent circuit model (see Note S2), and the charge transferred from each electrode at stages 1 and 3 can be written as

$$\Delta Q_{ring} = \frac{C_d Q_{FEP} + C_{FEP} Q_d}{C_d + C_{FEP}} \text{ and} \qquad \text{(Equation 2)}$$

$$\Delta Q_{circle} = -\frac{C_d Q_{FEP} + C_{FEP} Q_d}{C_d + C_{FEP},} \qquad \text{(Equation 3)}$$

where Q_{FEP} and Q_d are the charges stored in C_{FEP} and C_d, respectively. According to Equations 2 and 3, the negative charges migrate from the ring to the circle electrodes at stages 1 and 3 and travel back to the ring electrode at stages 2 and 4. The charge was measured in single-electrode configurations, where the measured charges were set to be half of the charge stored in each capacitor,[37] and the fitted values of C_d and C_{FEP} (Figure S4) were applied to Equations 2 and 3. The value of $|\Delta Q_{ring}| = |\Delta Q_{circle}|$ was determined to be 14.1 nC, comparable to the charge amount measured for the FDEG (Figure S3).

Optimizing the instantaneous output in FDEG

The magnitude of the outputs in the FDEG could be tuned by adjusting various parameters in the equivalent circuit model, such as the resistances, capacitances, charges, and switches in the closed-loop circuit. We examined the variation in the current peak as a function of droplet volume (Figures 2A and S5). The magnitude increases from 0.4 to 22.8 μA with an increase in the droplet volume from 0.1 to 2.4 mL, but a further increase in the droplet volume results in a decreased current peak value. The maximum peak occurs when the droplet size approximately matches the separation distance between the ring and circle electrodes. The peak values in response to differing droplet volumes suggest that the output peak can be manipulated by the resistance in the closed-loop circuit, in addition to capacitances and their charges. As depicted in Figure 2B, small droplets with respect to the gap lead to greater surface resistance, whereas decreasing water resistance and decreasing charge develop on the ring electrode surface. With a further increase in droplet size, the water bridge fully covers the gap (Figure S6), after which the output peak starts to rely only on water resistance. We modified the aforementioned model with variable resistances and charges (Note S3), and the model fit the experimental data, as shown in Figure 2A. To gain insight into the device scaling factor, we varied the length ratio of the gap-to-electrode diameter while matching the droplet size with the gap length (Figure S7) to rule out the effect of surface resistance. We found that the current peak exhibited a maximum value of 22.80 μA when the length ratio was approximately 0.7, which we attributed to the trade-off tendency between water resistance, R_{water}, and Q_d with increasing droplet size. This suggests the particular length ratio of a gap to a circular electrode when scaling up the device,

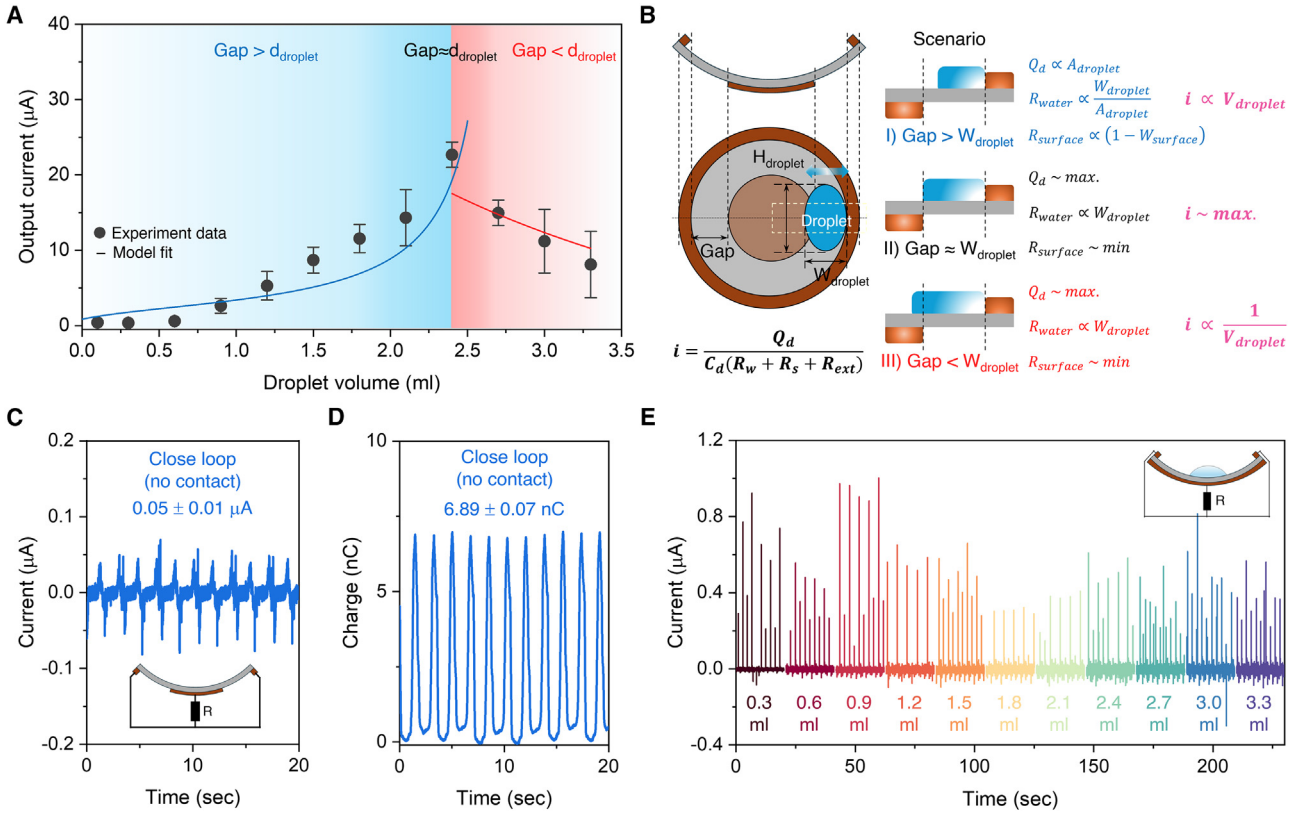

Figure 2. Figure of merit of the FDEG

(A) The instantaneous output currents as a function of the DI water droplet volume employed in the FDEG.

(B) Schematic of droplet behaviors differing in volume on the device surface and related parameters in the equivalent circuit.

(C and D) Output current (C) and generated charge (D) measured from the control device with similar capacitance on two electrodes for comparison, demonstrating the importance of a significant difference in capacitance.

(E) The output current yielded from the device featuring continuous switching on over the course of oscillation, highlighting that the process of instantaneous switching on and off is a critical factor in engendering an outstanding instantaneous output current.

demonstrating a voltage and current of 178.4 V and 100.7 μA, respectively, when the device scaled up by ~57% (Figure S8).

We postulate that the large difference in C_d and C_{FEP} in the closed-loop circuit is critical for inducing an increase in the current output. We designed a controlled closed-loop device with a ring electrode underneath the FEP layer to increase the capacitance of the ring electrode to a value similar to that of the circular electrode. No apparent instantaneous increases in peak density were observed when a droplet of 2.4 mL was rolled over the device (Figure 2C). We calculated the capacitance of the ring electrode as 0.216 nF using Equation 1 and the charges measured for the single-electrode configurations (Figure S9), which is two orders of magnitude larger than that of the ring electrode in the FDEG. The magnitude of the current peak is 456-fold less than that of the FDEG, while the amount of transferred charges is only 2.4 times less than that of the FDEG (Figure 2D), implying that similar capacitances of C_d and C_{FEP} in the control device substantially reduce the current output. We found that the process of switching plays an important role in the current peak, as the charge accumulated in the ring electrode can be discharged over the course of the switching process. We prepared a device in which the switch of the circuit was always on while the droplet touched the ring electrode as a proof of concept by fully covering the bottom surface of the FEP layer with the circle electrode. Although instantaneous current peaks in the range of 0.3–1 μA occur at the moment of contact with the ring electrode, the magnitude of the peaks is low and independent of the difference in droplet volume (Figure 2E). The reduction in peak magnitude may arise as a result of continuous balancing in charge developed in both electrodes while switching on. The fast switching of the circuit, which can be done by rapid oscillation, facilitates the boost of the current output (Figure S10), corroborating the importance of switching in yielding an increase in the current output.

Salt dependence of the instantaneous peak in the FDEG

The current peaks in the FDEG can be generated by aqueous droplets other than DI water. Figure 3A shows that a peak can reach 67.10 ± 13.78 μA when tap water is used, and an approximately 4-fold decrease (15.23 ± 8.42 μA) in the value is observed when seawater is used. We tested the FDEG using 50 different types of solutions, each containing a different salt type (LiCl, NaCl, $MgCl_2$, Na_2CO_3, and Na_2SO_4) and concentration (0.01, 0.05, 0.1, 0.5, 1, 5, 10, 50, 100, and 300 mM), which gives rise

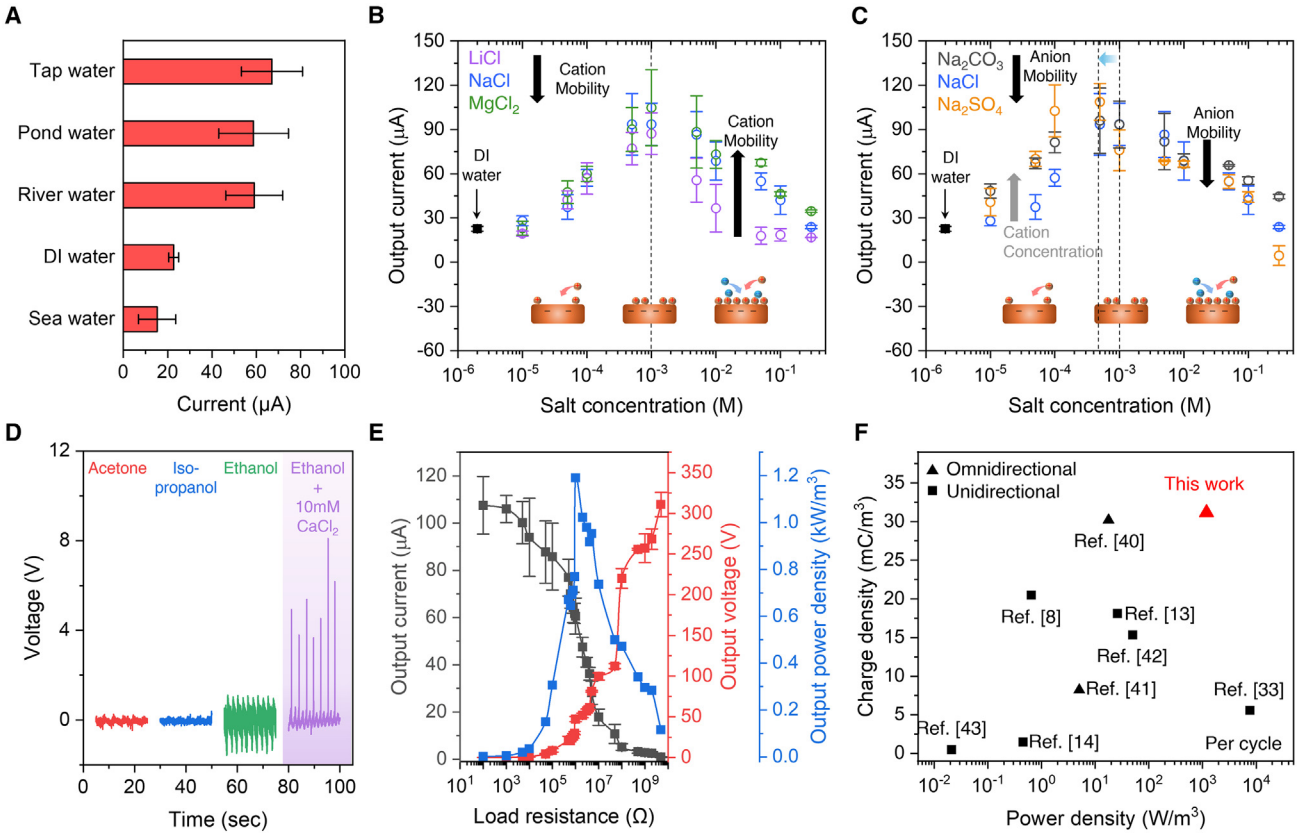

Figure 3. Effect of salinity on the instantaneous peak

(A) Instantaneous current peaks from the FDEG in contact with tap, pond, river, DI, and sea waters.

(B) Current output in the presence of differing concentrations of salts containing the same anion but varying cations. Cation mobility determines the intensity of the current output.

(C) Current output in the presence of differing concentrations of salts containing the same cation but varying anions, in which an increase in anion mobility gives rise to a decrease in current output.

(D) Salt addition to weak Brønsted acids, rendering the FDEG capable of producing the instantaneous current peak.

(E) Current output, voltage, and power from the FDEG in contact with 0.5 mM Na_2SO_4 solution as a function of load resistance. The power was normalized to the droplet volume used.

(F) Normalized charge and power densities of the FDEG (data from E) compared with literature data for state-of-the-art droplet-based TENGs, including unidirectional[8,13,14,33,42,43] and omnidirectional[40,41] modes. The power was normalized to the droplet volume used.

to variations in C_d and Q_d. As shown in Figures 3B and 3C, the peaks reach their maximum values at concentrations of 1 and 0.5 mM for droplets containing salts with monovalent and divalent anions, respectively. These values decrease with increasing concentration. Interestingly, the quantity of cations influences the amplitude of the instantaneous current peak prior to attaining the maximum current value, as well as the concentration at which the maximum current value occurs. The ion mobility is also responsible for determining the current peak beyond the critical concentration.

We attribute this behavior to the nature of the electrical double layer formation.[38] At low concentrations, elevating the concentration allows more cations to approach the negatively charged Cu surface to form an immobile Stern layer, which refers to an ion layer where ions are closest to the charged surface, affording the electrical double layer more charge to be stored. After establishing the compact Stern layer, both anions and cations migrate competitively to immobile cations in the diffuse layer. As the ion concentration increases, the charge retained within the electrical double layer is predominantly neutralized by anions, which is attributable to their mobility compared to that of cations.[39] Figure S11 illustrates the correlation between the charge produced by the Na_2SO_4 droplet and the behavior of the peak instantaneous current as a function of salt concentration. The capacitance of the electrical double layer seems to display minimal variance, as shown in Figure S12. These observations suggest that the Q_d factor affects the observed behavior of the peak. We found that the addition of salt to weak Brønsted acids, such as acetone, isopropanol, and ethanol, helps endow electricity generators with the ability to produce a sharp current peak (Figure 3D), suggesting that feeding cations into the solvent facilitates the storage of more charges in the electrical double layer.

To investigate the output power from the FDEG with salt droplets, variable resistors and aqueous droplets of 0.5 mM Na_2SO_4

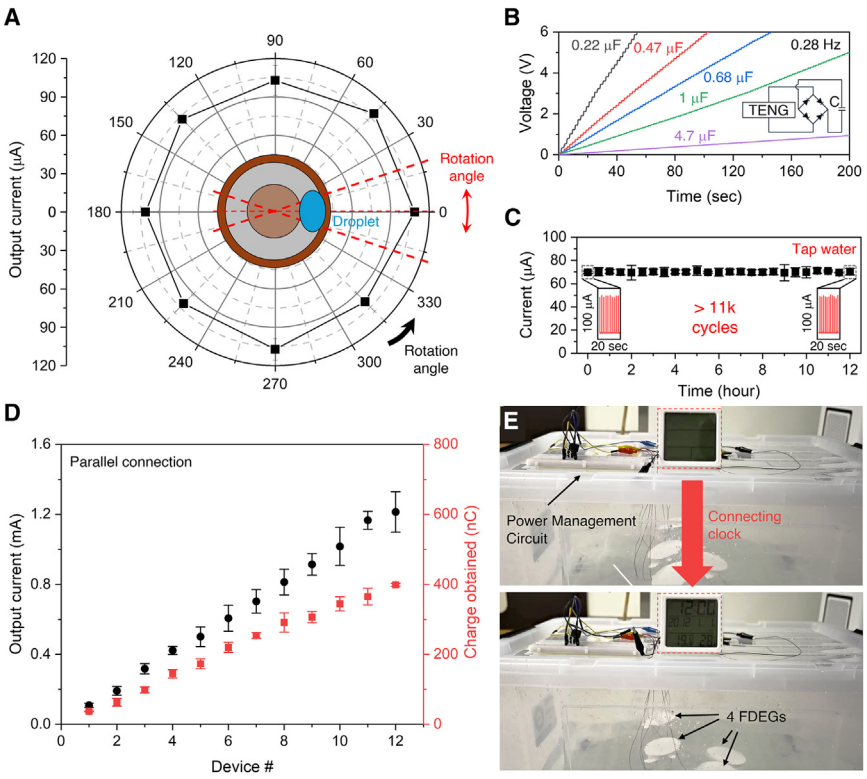

Figure 4. Practical applications of the FDEG

(A) Omnidirectionality of the FDEGs.

(B) Capacitive charging with the FDEG. The inset indicates an equivalent circuit.

(C) Stability of the FDEG over 11,000 cycles.

(D) Current and charge enhancements as a function of device number, from one to twelve devices, with parallel connections.

(E) Photo of the 4 FDEGs being driven in the "WAVE" bath along with the power management circuit. The power output from 4 FDEGs allows us to power an electronic clock.

were tested. The current amplitude decreased from 107.6 ± 12.2 μA with increasing external load due to the ohmic loss, whereas the output voltage exhibited the opposite trend, reaching up to 310.8 ± 14.9 V at a load of 5 GΩ (Figure 3E). The corresponding output power density reached a maximum of ~1,190.6 W/m^3, in which the output power density was normalized by the droplet volume used, at an external resistance of 1 MΩ. To our knowledge, this droplet-volumetric power density is higher than that reported to date for droplet-based TENGs that harvest omnidirectional wave energy (Figure 3F).[40,41] More importantly, our FDEG has been shown to outperform other droplet-based TENGs in terms of droplet-volumetric charge density (31.2 mC/m^3), which is advantageous for practical applications.[8,13,14,33,42,43] When our FDEG is tilted and lifted by waves, the potential energy of the device is converted into electrical energy, corresponding to $E_{potential} = mgh$ and $E_{electrical} = \int I^2(t)Rdt$, where m is the mass of the device, g is gravitational acceleration, and h is the height difference. $I(t)$ and R denote the time-variable current and external load resistance of each cycle, respectively. We estimated the energy conversion efficiency as $\eta = 83.4\%$ using the relation $\eta = E_{electrical}/E_{potential}$, which is comparable to the value reported for TENGs.[16,44]

Application demonstrations and durability tests

The symmetric device architecture of our FDEG resulted in stable energy harvesting from omnidirectional waving motions (Figure 4A), which is beneficial for open water wave energy harvesting, where wave conditions are seldom controlled (Figure S13; Video S1). We evaluated capacitor charging with our FDEG and rectifying unit, and capacitors of 0.22, 0.47, 0.68, 1, and 4.7 μF were stably charged to 1 V within 7.7, 16.8, 24.5, 44.3, and 213.2 s, respectively (Figure 4B). The rectified electrical output of the FDEG offers powering of 80 light-emitting diodes (LEDs) (Figure S14), and the electrical outputs of more than 11,000 cycles showcase its stability when in contact with tap water (Figure 4C). To verify the long-term stability of our FDEG upon exposure to extreme conditions, we tested the current output of the device after storing it in a convection oven for over 3 months at 60°C. As shown in Figure S15, the current output of FDEG was stable over a 12 h test after being in the oven for 3 months. This stability is due in large part to the inert nature of the FEP polymer,[45] which minimizes the degradation of the device even upon exposure to extreme conditions. The output current and charge generated can be improved by the parallel connection of multiple FDEGs, achieving up to 1.2 ± 0.1 mA and 0.4 μC, respectively, with 12 FDEGs (Figure 4D). Leveraging the charge generated from our FDEGs with a power management circuit consisting of a rectifier and a capacitor, we retarded the discharge time of the capacitor by up to 1 V compared to the discharge time without the FDEG device, and the capacitor maintained a constant voltage of 0.5 V even during continuous discharge (Figure S16), enough to power a calculator.

We investigated the performance of our FDEGs against random fluctuations of water in a plastic bath to simulate realistic wave conditions (Figure S17). Teflon tape was used to cover the FDEG as a customized lid (Figure S18A), and the device maintained its ability to float with the increased weight. The lid prevents the evaporation and leakage of droplets (Figure S18B) while also preventing the external water from permeating into the FDEG (Video S2). For the test, we applied a linear sliding force to the bath to create linear waves in the water. Although the current output exhibited a large variation in the range of 10–120 μA, the current observed was large and stable enough to power the LEDs and an electronic clock (Figures 4E and S19; Videos S3 and S4).

Through the examination of the acrylic bowl geometry, we calculated that the minimum tilting angle that could produce

Table 1. Design parameters and inertial characteristics for calculations

Draft/m	0.044
Pontoon mass/g	10.21
I_{xx}/g m^2	27.04
I_{yy}/g m^2	27.04
I_{zz}/g m^2	46.82

instantaneous power is determined to be approximately 46.4° (Figure S20A). Computational fluid dynamics (CFD) simulations were employed to gain insight into the tilt angle of the acrylic bowl upon exposure to the wave with a frequency and amplitude of 0.25 Hz and 0.7 m, respectively. When exposed to oscillating mild waves with an amplitude of 0.6 m, the acrylic bowl has been found to be tilted between 0° and 48.24° (Figure S20B). The tilting angle would increase to 64.2° when the wave amplitude was increased to 1.6 m (Figure S20C). Given that 90% of all waves are expected to be greater than an amplitude of 1 m if a steady wind of 55.56 km/h blew for 24 h over a fetch of 547 km,[46] we believe our FDEG will be mostly operational upon exposure to the typical ocean wave. More importantly, due to the size and inertia of droplets, a much lower tilting angle (~24°) is required to make our FDEG operational in empirical conditions (Figure S20D), enabling our FDEG to harvest wave energy with an even lower amplitude of 0.1 m. Our results demonstrate the potential of our FDEGs for harnessing natural wave energy as a renewable power resource for self-powered electronics.

Conclusion and outlook

We presented a FDEG constructed from asymmetric electrodes on a contact-electrification layer and a liquid droplet that outperforms conventional droplet-based electricity generators in terms of power and charge density. The difference in capacitance formed on each electrode, together with the switching of the circuit by the moving droplet, enhances the magnitude of the output current, while the amount of charge generated remains similar. Additional ion injection into the droplet improved the amount of charge generated, leading to an output power density of up to 1,190.6 W/m^3 and a charge density of 31.2 mC/m^3, breaking previous records for droplet-based TENGs. The potential of FDEGs for natural vibration energy harvesting was tested under realistic environmental conditions. These demonstrations of omnidirectionality, stability, and scalability can help enable these FDEGs to continuously power electrical devices, even under low-frequency mechanical stimuli.

The networks of FDEGs, constructed by linking millions of device units, are predicted to be a feasible strategy to realizing such a commercial power generation. With a single unit producing a power density of around 1.2 kW/m^3 under a wave frequency of 0.25 Hz, the FDEG network over 10 square kilometers with 10 cm intervals is expected to generate enough electricity of MW scale for a town. This trait particularly suggests that such a network could serve as a cost-effective energy platform beyond current renewable energy technologies, such as tidal, wind, and solar energy, given that minimum manufacturing and maintenance costs are required for TENG networks.[47] Future refinement and development of the FDEGs can help propel this toward commercial-scale power generation. The device size needs to be upscaled, and its droplet volume and salt concentration need optimization while keeping both cost and environmental implications in mind. The salt concentration is also needed to consider the phase transition temperature to secure a wide working temperature range. Despite the added lid fitted on the FDEG demonstrating minimal droplet leakage over a period of 140 h, there is room for enhancement in the stability of the FDEG performance. This can be achieved through comprehensive sealing of the device lid via device engineering, as the device's droplet evaporation may be influenced by real-world weather conditions such as temperature, humidity, and wind. The device outlined in this study, with future advancements, holds significant potential for progressing sustainable and widespread energy harvesting technologies from natural vibrations, including but not limited to open ocean waves, pendulum swings, and cantilever oscillations.

METHODS

Fabrication of the FDEG

The basic structure of the FDEG comprises a thin FEP film with a diameter of 72.3 mm (FEP, Taizhou Chenguang Plastic Industry) along with ring (width of 3 mm) and circular Cu electrodes at the circumference and center, respectively. The adhesive ring electrode was attached to the top of the FEP layer, while the adhesive circle electrode was located underneath the FEP layer. The FDEG was positioned on the inner surface of an acrylic hemispheric bowl with a diameter of 70 mm and depth of 15 mm, allowing the electricity generator to float and be waved. All FDEGs were washed with ethanol three times to remove the precharges, followed by mild annealing at 80°C overnight. A liquid droplet sliding off the top of the FEP layer serves as a counter-contact electrification material.

Characterization methods

An oscilloscope (Agilent DSO-X-2012A) equipped with a preamplifier (SRS SR-570) was utilized to measure the output voltage and current from the FDEG. The voltage and current of the FDEG were measured with high-impedance (100 MΩ) and low-impedance (50 Ω) probes, respectively, without connecting external loads. A digital multimeter (Keithley 6514) was used to analyze the generated charge. The wettability and surface morphology of the FEP films were investigated using a Kruss DSA20E easy drop contact angle measurement system and a field-emission scanning electron microscope (Hitachi S4800), respectively. The electronic calculator and clock were directly connected to either individual or parallelly combined nanogenerators with a power management circuit featuring a rectifier and a capacitor.

CFD calculations

The hydrodynamic model of the FDEG was established using SolidWorks 2023 and then imported into ANSYS-AQWA to analyze its response to regular waves. The model size was similar to that used in the experimental tests, with the specific design parameters and inertial characteristics shown in Table 1.

The FDEG was placed in a 50 × 50 × 5 m^3 water domain, the water density was set to 1025 kg/m^3 to mimic seawater density, and the gravitational acceleration was set to 9.8 m/s^2. A regular wave response was applied to the system, with a frequency of 0.25 Hz to simulate typical wave frequencies and a wave amplitude of 0.1 m. During the simulation, the total duration was set to 10 s, with a time step of 0.001 s. Subsequently, ANSYS-AQWA was used to perform a time-domain analysis to simulate the angular response of the FDEG oscillations.

RESOURCE AVAILABILITY

Lead contact

Requests for further information and resources should be directed to and will be fulfilled by the lead contact, Dong-Myeong Shin (dmshin@hku.hk).

Materials availability

The materials in this study will be made available on request.

Data and code availability

The data in this study are available within the paper and its supplemental information.

ACKNOWLEDGMENTS

The authors acknowledge the financial support of the General Research Fund of the Research Grants Council of the Hong Kong Special Administrative Region, China, under award no. 27202920.

AUTHOR CONTRIBUTIONS

D.-M.S. and J.Z. conceived the overall research goals and aims. D.-M.S. and J.Z. designed the experiments. J.Z. fabricated the devices and performed the characterization with help from X.M., Z.D., J.G., E.K., and H.Z. D.-M.S. and J.Z. performed the data analysis and organized the results. All the authors contributed to writing the manuscript.

DECLARATION OF INTERESTS

The authors declare the following financial interests/personal relationships, which may be considered potential competing interests: the University of Hong Kong has applied for a patent (US application no. 63/650,159) on some of the technologies discussed herein, on which some of the authors of this paper are listed as coinventors.

SUPPLEMENTAL INFORMATION

Supplemental information can be found online at https://doi.org/10.1016/j.device.2024.100653.

Received: September 24, 2024
Revised: October 6, 2024
Accepted: December 5, 2024
Published: January 1, 2025

REFERENCES

1. Fan, F.-R., Tian, Z.-Q., and Wang, Z.L. (2012). Flexible triboelectric nanogenerator. Nano Energy *1*, 328–334. https://doi.org/10.1016/j.nanoen.2012.01.004.
2. Jeong, J., Jeon, S., Ma, X., Kwon, Y.W., Shin, D.-M., and Hong, S.W. (2021). A Sustainable and flexible microbrush-faced triboelectric generator for portable/wearable applications. Adv. Mater. *33*, 2102530. https://doi.org/10.1002/adma.202102530.
3. Tang, W., Jiang, T., Fan, F.R., Yu, A.F., Zhang, C., Cao, X., and Wang, Z.L. (2015). Liquid-Metal Electrode for High-Performance Triboelectric Nanogenerator at an Instantaneous Energy Conversion Efficiency of 70.6%. Adv. Funct. Mater. *25*, 3718–3725. https://doi.org/10.1002/adfm.201501331.
4. Yuan, Z., Wang, C., Xi, J., Han, X., Li, J., Han, S.-T., Gao, W., and Pan, C. (2021). Spherical Triboelectric Nanogenerator with Dense Point Contacts for Harvesting Multidirectional Water Wave and Vibration Energy. ACS Energy Lett. *6*, 2809–2816. https://doi.org/10.1021/acsenergylett.1c01092.
5. Ying, Q., Wu, J., and Liu, C. (2024). Multi-Track Triboelectric Nanogenerator Toward Omnidirectional Ocean Wave Energy Harvesting. Adv. Mater. Technol. *9*, 2301824. https://doi.org/10.1002/admt.202301824.
6. Yang, X., Xu, L., Lin, P., Zhong, W., Bai, Y., Luo, J., Chen, J., and Wang, Z.L. (2019). Macroscopic self-assembly network of encapsulated high-performance triboelectric nanogenerators for water wave energy harvesting. Nano Energy *60*, 404–412. https://doi.org/10.1016/j.nanoen.2019.03.054.
7. Pang, Y., Fang, Y., Su, J., Wang, H., Tan, Y., and Cao, C.C. (2023). Soft Ball-Based Triboelectric-Electromagnetic Hybrid Nanogenerators for Wave Energy Harvesting. Adv. Mater. Technol. *8*, 2201246. https://doi.org/10.1002/admt.202201246.
8. Wei, X., Zhao, Z., Zhang, C., Yuan, W., Wu, Z., Wang, J., and Wang, Z.L. (2021). All-Weather Droplet-Based Triboelectric Nanogenerator for Wave Energy Harvesting. ACS Nano *15*, 13200–13208. https://doi.org/10.1021/acsnano.1c02790.
9. Liu, L., Yang, X., Zhao, L., Hong, H., Cui, H., Duan, J., Yang, Q., and Tang, Q. (2021). Nodding Duck Structure Multitrack Directional Freestanding Triboelectric Nanogenerator toward Low-Frequency Ocean Wave Energy Harvesting. ACS Nano *15*, 9412–9421. https://doi.org/10.1021/acsnano.1c00345.
10. Wang, X., Niu, S., Yin, Y., Yi, F., You, Z., and Wang, Z.L. (2015). Triboelectric Nanogenerator Based on Fully Enclosed Rolling Spherical Structure for Harvesting Low-Frequency Water Wave Energy. Adv. Energy Mater. *5*, 1501467. https://doi.org/10.1002/aenm.201501467.
11. Ahmed, A., Saadatnia, Z., Hassan, I., Zi, Y., Xi, Y., He, X., Zu, J., and Wang, Z.L. (2017). Self-Powered Wireless Sensor Node Enabled by a Duck-Shaped Triboelectric Nanogenerator for Harvesting Water Wave Energy. Adv. Energy Mater. *7*, 1601705. https://doi.org/10.1002/aenm.201601705.
12. Cheng, P., Guo, H., Wen, Z., Zhang, C., Yin, X., Li, X., Liu, D., Song, W., Sun, X., Wang, J., and Wang, Z.L. (2019). Largely enhanced triboelectric nanogenerator for efficient harvesting of water wave energy by soft contacted structure. Nano Energy *57*, 432–439. https://doi.org/10.1016/j.nanoen.2018.12.054.
13. Wu, H., Wang, Z., and Zi, Y. (2021). Multi-Mode Water-Tube-Based Triboelectric Nanogenerator Designed for Low-Frequency Energy Harvesting with Ultrahigh Volumetric Charge Density. Adv. Energy Mater. *11*, 2100038. https://doi.org/10.1002/aenm.202100038.
14. Zhang, Q., He, M., Pan, X., Huang, D., Long, H., Jia, M., Zhao, Z., Zhang, C., Xu, M., and Li, S. (2022). High-performance liquid–solid-solid tubular triboelectric nanogenerator for scavenging water wave energy. Nano Energy *103*, 107810. https://doi.org/10.1016/j.nanoen.2022.107810.
15. Pan, L., Wang, J., Wang, P., Gao, R., Wang, Y.-C., Zhang, X., Zou, J.-J., and Wang, Z.L. (2018). Liquid-FEP-based U-tube triboelectric nanogenerator for harvesting water-wave energy. Nano Res. *11*, 4062–4073. https://doi.org/10.1007/s12274-018-1989-9.
16. Zhou, J., Ma, X., Gao, J., Kim, E., Deng, Z., Rao, Q., Li, W.-D., Ki, D.-K., and Shin, D.-M. (2024). Switchable Power Generation in Triboelectric Nanogenerator Toward Chip-Less Wearable Power Module Applications. Small *20*, 2306980. https://doi.org/10.1002/smll.202470239.
17. Zhang, C., He, L., Zhou, L., Yang, O., Yuan, W., Wei, X., Liu, Y., Lu, L., Wang, J., and Wang, Z.L. (2021). Active resonance triboelectric nanogenerator for harvesting omnidirectional water-wave energy. Joule *5*, 1613–1623. https://doi.org/10.1016/j.joule.2021.04.016.

18. Zhang, C., Zhou, L., Cheng, P., Liu, D., Zhang, C., Li, X., Li, S., Wang, J., and Wang, Z.L. (2021). Bifilar-Pendulum-Assisted Multilayer-Structured Triboelectric Nanogenerators for Wave Energy Harvesting. Adv. Energy Mater. *11*, 2003616. https://doi.org/10.1002/aenm.202003616.

19. An, J., Wang, Z.M., Jiang, T., Liang, X., and Wang, Z.L. (2019). Whirling-Folded Triboelectric Nanogenerator with High Average Power for Water Wave Energy Harvesting. Adv. Funct. Mater. *29*, 1904867. https://doi.org/10.1002/adfm.201904867.

20. Lin, Z., Zhang, B., Xie, Y., Wu, Z., Yang, J., and Wang, Z.L. (2021). Elastic-Connection and Soft-Contact Triboelectric Nanogenerator with Superior Durability and Efficiency. Adv. Funct. Mater. *31*, 2105237. https://doi.org/10.1002/adfm.202105237.

21. Hu, Y., Yang, J., Jing, Q., Niu, S., Wu, W., and Wang, Z.L. (2013). Triboelectric Nanogenerator Built on Suspended 3D Spiral Structure as Vibration and Positioning Sensor and Wave Energy Harvester. ACS Nano *7*, 10424–10432. https://doi.org/10.1021/nn405209u.

22. Jiang, T., Yao, Y., Xu, L., Zhang, L., Xiao, T., and Wang, Z.L. (2017). Spring-assisted triboelectric nanogenerator for efficiently harvesting water wave energy. Nano Energy *31*, 560–567. https://doi.org/10.1016/j.nanoen.2016.12.004.

23. Xiao, T.X., Jiang, T., Zhu, J.X., Liang, X., Xu, L., Shao, J.J., Zhang, C.L., Wang, J., and Wang, Z.L. (2018). Silicone-Based Triboelectric Nanogenerator for Water Wave Energy Harvesting. ACS Appl. Mater. Interfaces *10*, 3616–3623. https://doi.org/10.1021/acsami.7b17239.

24. Xi, F., Pang, Y., Liu, G., Wang, S., Li, W., Zhang, C., and Wang, Z.L. (2019). Self-powered intelligent buoy system by water wave energy for sustainable and autonomous wireless sensing and data transmission. Nano Energy *61*, 1–9. https://doi.org/10.1016/j.nanoen.2019.04.026.

25. Zhang, B., Xu, W., Peng, L., Li, Y., Zhang, W., and Wang, Z. (2024). Nature-inspired interfacial engineering for energy harvesting. Nat. Rev. Electr. Eng. *1*, 218–233. https://doi.org/10.1038/s44287-024-00029-6.

26. Zhang, Q., Li, Y., Cai, H., Yao, M., Zhang, H., Guo, L., Lv, Z., Li, M., Lu, X., Ren, C., et al. (2021). A single-droplet electricity generator achieves an ultrahigh output over 100 V without pre-charging. Adv. Mater. *33*, 2105761. https://doi.org/10.1002/adma.202105761.

27. Wang, X., Fang, S., Tan, J., Hu, T., Chu, W., Yin, J., Zhou, J., and Guo, W. (2021). Dynamics for droplet-based electricity generators. Nano Energy *80*, 105558. https://doi.org/10.1016/j.nanoen.2020.105558.

28. Li, Z., Yang, D., Zhang, Z., Lin, S., Cao, B., Wang, L., Wang, Z.L., and Yin, F. (2022). A droplet-based electricity generator for large-scale raindrop energy harvesting. Nano Energy *100*, 107443. https://doi.org/10.1016/j.nanoen.2022.107443.

29. Wang, L., Song, Y., Xu, W., Li, W., Jin, Y., Gao, S., Yang, S., Wu, C., Wang, S., and Wang, Z. (2021). Harvesting energy from high-frequency impinging water droplets by a droplet-based electricity generator. EcoMat *3*, e12116. https://doi.org/10.1002/eom2.12116.

30. Zhang, N., Zhang, H., Xu, W., Gu, H., Ye, S., Zheng, H., Song, Y., Wang, Z., and Zhou, X. (2022). A droplet-based electricity generator with ultrahigh instantaneous output and short charging time. Droplet *1*, 56–64. https://doi.org/10.1002/dro2.10.

31. He, P., Ding, J., Lei, L., and Tao, W.-Q. (2024). A four-electrode droplet triboelectric nanogenerator providing multimodal output. Cell Reports Physical Science *5*, 101800. https://doi.org/10.1016/j.xcrp.2024.101800.

32. Jang, S., Shah, S.A., Lee, J., Cho, S., Kam, D., Ra, Y., Lee, D., Khawar, M.R., Yoo, D., Ahmad, A., and Choi, D. (2024). Beyond Metallic Electrode: Spontaneous Formation of Fluidic Electrodes from Operational Liquid in Highly Functional Droplet-Based Electricity Generator. Adv. Mater. *36*, 2403090. https://doi.org/10.1002/adma.202403090.

33. Zhou, Q., Wang, B., Gao, A., Xu, W., Zhou, K., Pan, J., Meng, G., Pan, C., and Xia, F. (2022). Solution-Tube-Based Volume Effect Triboelectric Nanogenerator with Salt and pH Sensitivity. Adv. Funct. Mater. *32*, 2209100. https://doi.org/10.1002/adfm.202209100.

34. Xu, W., Zheng, H., Liu, Y., Zhou, X., Zhang, C., Song, Y., Deng, X., Leung, M., Yang, Z., Xu, R.X., et al. (2020). A droplet-based electricity generator with high instantaneous power density. Nature *578*, 392–396. https://doi.org/10.1038/s41586-020-1985-6.

35. Li, Y., Qin, X., Feng, Y., Song, Y., Yi, Z., Zheng, H., Zhou, P., Wu, C., Yang, S., Wang, L., et al. (2024). A droplet-based electricity generator incorporating Kelvin water dropper with ultrahigh instantaneous power density. Droplet *3*, e91. https://doi.org/10.1002/dro2.91.

36. Burgo, T.A., Galembeck, F., and Pollack, G.H. (2016). Where is water in the triboelectric series? J. Electrost. *80*, 30–33. https://doi.org/10.1016/j.elstat.2016.01.002.

37. Niu, S., Liu, Y., Wang, S., Lin, L., Zhou, Y.S., Hu, Y., and Wang, Z.L. (2014). Theoretical Investigation and Structural Optimization of Single-Electrode Triboelectric Nanogenerators. Adv. Funct. Mater. *24*, 3332–3340. https://doi.org/10.1002/adfm.201303799.

38. Chu, B., Biriukov, D., Bischoff, M., Předota, M., Roke, S., and Marchioro, A. (2023). Evolution of the electrical double layer with electrolyte concentration probed by second harmonic scattering. Faraday Discuss *246*, 407–425. https://doi.org/10.1039/D3FD00036B.

39. Atkins, P., de Paula, J., and Keeler, J. (2023). Atkins' Physical Chemistry, 13th ed. (Oxford University Press).

40. Zhang, H., Chen, Y., Deng, Z., Deng, L., Xing, J., Yang, Q., Mi, H., Zhang, H., Xu, C., Shen, X., et al. (2024). A high-output performance disc-shaped liquid–solid triboelectric nanogenerator for harvesting omnidirectional ultralow-frequency natural vibration energy. Nano Energy *121*, 109243. https://doi.org/10.1016/j.nanoen.2023.109243.

41. Xu, Q., Shang, C., Ma, H., Hong, Q., Li, C., Ding, S., Xue, L., Sun, X., Pan, Y., Sugahara, T., et al. (2023). A guided-liquid-based hybrid triboelectric nanogenerator for omnidirectional and high-performance ocean wave energy harvesting. Nano Energy *109*, 108240. https://doi.org/10.1016/j.nanoen.2023.108240.

42. Zhou, H., Dong, J., Liu, H., Zhu, L., Xu, C., He, X., Zhang, S., and Song, Q. (2022). The coordination of displacement and conduction currents to boost the instantaneous power output of a water-tube triboelectric nanogenerator. Nano Energy *95*, 107050. https://doi.org/10.1016/j.nanoen.2022.107050.

43. Shi, Q., Wang, H., Wu, H., and Lee, C. (2017). Self-powered triboelectric nanogenerator buoy ball for applications ranging from environment monitoring to water wave energy farm. Nano Energy *40*, 203–213. https://doi.org/10.1016/j.nanoen.2017.08.018.

44. Zheng, Y., Liu, T., Wu, J., Xu, T., Wang, X., Han, X., Cui, H., Xu, X., Pan, C., and Li, X. (2022). Energy Conversion Analysis of Multilayered Triboelectric Nanogenerators for Synergistic Rain and Solar Energy Harvesting. Adv. Mater. *34*, 2202238. https://doi.org/10.1002/adma.202202238.

45. Nag, A., Baksi, A., Ghosh, J., Kumar, V., Bag, S., Mondal, B., Ahuja, T., and Pradeep, T. (2019). Tribochemical degradation of polytetrafluoroethylene in water and generation of nanoplastics. ACS Sustain. Chem. Eng. *7*, 17554–17558. https://doi.org/10.1021/acssuschemeng.9b03573.

46. Dorn, W.V. (2009). Oceanography and Seamanship (Cornell Maritime Press).

47. Wang, Z.L., Jiang, T., and Xu, L. (2017). Toward the blue energy dream by triboelectric nanogenerator networks. Nano Energy *39*, 9–23. https://doi.org/10.1016/j.nanoen.2017.06.035.